

# Domain wall constraints on the doublet left-right symmetric model from pulsar timing array data

Dhruv Ringe<sup>a1</sup>

<sup>1</sup>*Department of Physics, Indian Institute of Technology Indore,  
Khandwa Road, Simrol, Indore, Madhya Pradesh-453552, India*

## Abstract

Recent evidence of a stochastic gravitational wave (GW) background found by NANOGrav and other pulsar timing array (PTA) collaborations has inspired many studies looking for possible sources. We consider the hypothesis that the GW signature is produced by domain walls (DWs) arising in the doublet left-right symmetric model (DLRSM) due to the spontaneous breaking of the discrete parity symmetry. The DW network consists of two types of DWs, namely  $Z_2$  and  $LR$  DWs, which have different surface tensions. We find kink solutions for both types of DWs and obtain the parametric dependence of the surface tension. Considering the GW signal from the DLRSM DW model with and without the contribution from supermassive black hole binaries, we perform a Bayesian analysis using the PTA data to estimate the posterior distribution and identify best-fit parameter ranges. The PTA data favors a parity-breaking scale of  $\mathcal{O}(10^5)$  GeV, and a biased potential  $V_{\text{bias}} \sim (\mathcal{O}(100) \text{ MeV})^4$ . The model with only DLRSM DWs is slightly favored over the model where additional SMBHB contribution is considered.

arXiv:2407.14075v1 [hep-ph] 19 Jul 2024

---

<sup>a</sup> phd1901151004@iiti.ac.in

## I. INTRODUCTION

The 15-year dataset (NG15) of the NANOGrav collaboration [1] shows compelling evidence of a stochastic gravitational wave background (SGWB) at nanoHertz frequencies. This evidence has been corroborated at varying significance levels by other pulsar timing arrays (PTAs) such as the European Pulsar Timing Array (EPTA) in collaboration with the Indian Pulsar Timing Array (InPTA) [2], Parkes Pulsar Timing Array (PPTA) [3], which are all part of the International Pulsar Timing Array (IPTA) consortium. While more data is needed to claim a discovery, discussing the possible sources of such a SGWB is interesting. The standard astrophysical interpretation, of the SGWB produced by in-spiralling supermassive black hole binaries (SMBHBs) scattered across the universe, is in slight tension with the data [1, 4–9]. Other explanations of cosmological origin have been discussed in the literature, including the gravitational waves (GWs) from the density perturbations after inflation [10–21], first-order phase transitions [22–34], and topological defects such as domain walls (DWs) [35–45] and cosmic strings [46–55].

Comparative analyses of the possible SGWB sources reveal that many of these models provide a better fit compared to the standard SMBHB interpretation [56–58]. In this paper, we consider DWs as the possible source of the signal, for which the Bayes factor is  $\mathcal{O}(10)$  when compared to the fiducial SMBHB model [56]. From the particle physics perspective, DWs are formed when a discrete symmetry is spontaneously broken. The GW spectrum from DWs depends on the surface tension,  $\sigma$ , of the walls, and the bias potential,  $V_{\text{bias}}$ . The PTA data is compatible with DWs for values roughly,  $\sigma \sim (100 \text{ TeV})^3$ , and the bias,  $V_{\text{bias}} \sim (100 \text{ MeV})^4$  [35]. A microscopic model for DWs at the electroweak (EW) scale,  $v_{\text{EW}} \sim 246.02 \text{ GeV}$ , cannot yield DWs with such a high surface tension, and thus a viable microscopic DW model must incorporate high-scale physics. Given that the EW interactions in the standard model (SM) maximally violate parity, high-scale extensions of SM that respect the parity symmetry,  $\mathcal{P}$ , provide an interesting way to generate DWs with sufficiently large surface tension.

Left-right symmetric models (LRSMs) [59–63] are well-motivated extensions of the standard model (SM) where the gauge group is extended from  $\mathcal{G}_{\text{SM}} = SU(3)_c \times SU(2)_L \times U(1)_Y$  to  $\mathcal{G}_{\text{LRSM}} = SU(3)_c \times SU(2)_L \times SU(2)_R \times U(1)_{B-L}$ . An additional discrete  $\mathcal{P}$  symmetry can be easily incorporated into  $\mathcal{G}_{\text{LRSM}}$ , allowing for the possibility of DW formation. The various realizations of LRSM differ from each other, depending on the scalars involved in the spontaneous breaking of  $\mathcal{G}_{\text{LRSM}}$  to  $\mathcal{G}_{\text{SM}}$ . They also differ in the mechanism of fermion mass generation. A widely studied realization is the triplet LRSM (TLRSM), where the scalar sector involves two triplets and a bidoublet [64–66]. When the scalar sector contains two doublets and a bidoublet, it is called the doublet LRSM (DLRSM) [63, 67]. Other versions of LRSM are also studied in the literature [68–73]. It was recently shown that the pattern of electroweak symmetry breaking (EWSB) in DLRSM can be quite different from the other versions of LRSM, with interesting consequences from precision observables [74] and Higgs

data [75].

In this paper, we study the DWs arising in parity-symmetric DLRSM. Previous discussions on DWs in LRSM [40, 76–83] mainly centered around TLRSM. In refs. [76, 82], the kink solutions for ‘left-right’ ( $LR$ ) DWs were presented for a few benchmark points. The GW signature was studied in refs. [40, 77], where the benchmarks were chosen based on an approximate dependence of the DW surface tension without explicitly solving the kink equations. In this paper, we show that two types of DWs are formed in DLRSM, namely,  $Z_2$  and  $LR$  DWs, with different surface tensions. For both types, we solve the kink equations to obtain the parametric dependence of the DW surface tension and show that the  $Z_2$  DWs are unstable. We then obtain the GW signature in terms of the DLRSM parameters. While qualitative similarity is expected in the GW signature of DWs from DLRSM and TLRSM, we perform a Bayesian analysis on the PTA data to constrain the model parameters. We consider the GW spectrum from DLRSM DWs with and without the contribution from SMBHBs. The discussion of this paper can be easily carried over to TLRSM.

In Sec. II, we briefly discuss the scalar potential of the  $\mathcal{P}$ -symmetric DLRSM. In Sec. III, we discuss the vacuum structure of the DLRSM effective potential and study the DW solutions. In Sec. IV, we discuss the GW spectrum resulting from DLRSM DWs. We present our results in Sec. V, where we perform the Markov chain Monte Carlo (MCMC) analysis, and discuss the detection prospects at upcoming GW observatories. Finally, we summarize our findings and make concluding remarks in Sec. VI.

## II. THE MODEL

The gauge group of parity-symmetric DLRSM is,

$$\mathcal{G}_{\text{LRSM}} = \mathcal{P} \times SU(3)_c \times SU(2)_L \times SU(2)_R \times U(1)_{B-L}.$$

For an overview of DLRSM, please refer to [63, 67, 74]. The scalar sector has a complex bi-doublet  $\Phi$ , and two doublets  $\chi_L$  and  $\chi_R$ . The scalar multiplets are,

$$\Phi = \begin{pmatrix} \phi_1^0 & \phi_2^+ \\ \phi_1^- & \phi_2^0 \end{pmatrix} \sim (1, 2, 2, 0), \quad \chi_L = \begin{pmatrix} \chi_L^+ \\ \chi_L^0 \end{pmatrix} \sim (1, 2, 1, 1), \quad \text{and} \quad \chi_R = \begin{pmatrix} \chi_R^+ \\ \chi_R^0 \end{pmatrix} \sim (1, 1, 2, 1), \quad (2.1)$$

where the parentheses indicate the representation of the multiplets under  $SU(3)_c$ ,  $SU(3)_L$ ,  $SU(3)_R$ , and  $U(1)_{B-L}$  respectively. The group  $\mathcal{P}$  denotes the discrete parity symmetry under the exchange  $L \leftrightarrow R$ , with the action given by,

$$\mathcal{P} : Q_L \leftrightarrow Q_R, \quad l_L \leftrightarrow l_R, \quad \chi_L \leftrightarrow \chi_R, \quad \Phi \leftrightarrow \Phi^\dagger, \quad (2.2)$$

where  $Q_L$ ,  $Q_R$ ,  $l_L$ ,  $l_R$  are the left and right-handed quark and lepton doublets respectively [74]. The  $\mathcal{P}$  symmetry imposes the condition  $g_L = g_R$  on the  $SU(2)_L$  and  $SU(2)_R$

gauge couplings. The scalar potential is given by [74],

$$\begin{aligned}
V &= V_\chi + V_{\chi\Phi} + V_\Phi, \\
V_\chi &= -\mu_3^2 [\chi_L^\dagger \chi_L + \chi_R^\dagger \chi_R] + \rho_1 [(\chi_L^\dagger \chi_L)^2 + (\chi_R^\dagger \chi_R)^2] + \rho_2 \chi_L^\dagger \chi_L \chi_R^\dagger \chi_R, \\
V_{\chi\Phi} &= \mu_4 [\chi_L^\dagger \Phi \chi_R + \chi_R^\dagger \Phi^\dagger \chi_L] + \mu_5 [\chi_L^\dagger \tilde{\Phi} \chi_R + \chi_R^\dagger \tilde{\Phi}^\dagger \chi_L] \\
&\quad + \alpha_1 \text{Tr}(\Phi^\dagger \Phi) [\chi_L^\dagger \chi_L + \chi_R^\dagger \chi_R] + \left\{ \frac{\alpha_2}{2} [\chi_L^\dagger \chi_L \text{Tr}(\tilde{\Phi} \Phi^\dagger) + \chi_R^\dagger \chi_R \text{Tr}(\tilde{\Phi}^\dagger \Phi)] + \text{h.c.} \right\} \\
&\quad + \alpha_3 [\chi_L^\dagger \Phi \Phi^\dagger \chi_L + \chi_R^\dagger \Phi^\dagger \Phi \chi_R] + \alpha_4 [\chi_L^\dagger \tilde{\Phi} \tilde{\Phi}^\dagger \chi_L + \chi_R^\dagger \tilde{\Phi}^\dagger \tilde{\Phi} \chi_R], \\
V_\Phi &= -\mu_1^2 \text{Tr}(\Phi^\dagger \Phi) - \mu_2^2 [\text{Tr}(\tilde{\Phi} \Phi^\dagger) + \text{Tr}(\tilde{\Phi}^\dagger \Phi)] + \lambda_1 [\text{Tr}(\Phi^\dagger \Phi)]^2 \\
&\quad + \lambda_2 [[\text{Tr}(\tilde{\Phi} \Phi^\dagger)]^2 + [\text{Tr}(\tilde{\Phi}^\dagger \Phi)]^2] + \lambda_3 \text{Tr}(\tilde{\Phi} \Phi^\dagger) \text{Tr}(\tilde{\Phi}^\dagger \Phi) \\
&\quad + \lambda_4 \text{Tr}(\Phi^\dagger \Phi) [\text{Tr}(\tilde{\Phi} \Phi^\dagger) + \text{Tr}(\tilde{\Phi}^\dagger \Phi)], \tag{2.3}
\end{aligned}$$

where  $\tilde{\Phi} \equiv \sigma_2 \Phi^* \sigma_2$ , and we take all parameters to be real. The pattern of symmetry breaking is:

$$\mathcal{P} \times SU(2)_L \times SU(2)_R \times U(1)_{B-L} \xrightarrow{\langle \chi_R \rangle} SU(2)_L \times U(1)_Y \xrightarrow{\langle \Phi \rangle, \langle \chi_L \rangle} U(1)_{\text{em}}.$$

The following charge-preserving and  $CP$ -preserving  $vev$  structure achieves the desired symmetry-breaking pattern:

$$\langle \Phi \rangle = \frac{1}{\sqrt{2}} \begin{pmatrix} \kappa_1 & 0 \\ 0 & \kappa_2 \end{pmatrix}, \quad \langle \chi_L \rangle = \frac{1}{\sqrt{2}} \begin{pmatrix} 0 \\ v_L \end{pmatrix}, \quad \langle \chi_R \rangle = \frac{1}{\sqrt{2}} \begin{pmatrix} 0 \\ v_R \end{pmatrix}. \tag{2.4}$$

The  $vevs$   $\kappa_1, \kappa_2$  and  $v_L$  follow the relation,  $\kappa_1^2 + \kappa_2^2 + v_L^2 = v_{\text{EW}}^2$ , where  $v_{\text{EW}} = 246.02 \text{ GeV}$ . The absence of a right-handed gauge boson in collider searches [84] dictates the hierarchy of scales in DLRSM:  $v_R \gg \kappa_1, \kappa_2, v_L$ . Since the potential is parity-symmetric, an alternative hierarchy where  $v_L \gg \kappa_1, \kappa_2, v_R$ , is also possible but is not realized in nature. We denote the  $\mathcal{P}$ -symmetry breaking scale by  $v_0$ , such that  $v_0 \gg v_{\text{EW}}$ . In the next section, we discuss how spontaneous breaking of the discrete  $\mathcal{P}$ -symmetry gives rise to regions of disconnected vacua separated by DWs.

### III. DOMAIN WALLS IN DLRSM

The existence of DWs can be inferred from the minima of the effective potential in the  $v_R - v_L$  plane. The tree-level effective potential of DLRSM is,

$$V_0 \equiv V_\chi(\langle \chi_L \rangle, \langle \chi_R \rangle) + V_{\chi\Phi}(\langle \chi_L \rangle, \langle \chi_R \rangle, \langle \Phi \rangle) + V_\Phi(\langle \Phi \rangle). \tag{3.1}$$

The contributions to the one-loop finite temperature effective potential were discussed in ref. [85]. A thorough analysis would require numerically calculating the full one-loop effective potential. Here we make some approximations to simplify the discussion. Symbolically,

$$V_{\text{eff}} = V_0 + V_1 + V_{1T}, \tag{3.2}$$

where  $V_1$  and  $V_{1T}$  are the one-loop zero-temperature and finite temperature corrections respectively. The effective potential obeys the symmetry of the tree-level potential. While we can always fix the zero-temperature minima and masses at their tree-level values by adding a finite counter-term to  $V_1$ , the role of  $V_{1T}$  should be analyzed.  $V_{1T}$  has the form,

$$V_{1T}(\phi, T) = \sum_{i \in \text{heavy}} n_i \frac{T^4}{2\pi^2} J_{b/f} \left( \frac{m_i^2(\phi)}{T^2} \right) + \sum_{i \in \text{light}} n_i \frac{T^4}{2\pi^2} J_{b/f} \left( \frac{m_i^2(\phi)}{T^2} \right), \quad (3.3)$$

where the sum runs over all fields, generically labeled by  $\phi$ . The term ‘heavy’ denotes  $v_0$ -scale fields  $\chi_L, \chi_R$ , and the gauge bosons,<sup>1</sup>  $W_{L,R}^\pm, Z_{L,R}$ . Similarly, ‘light’ denotes the EW-scale fields including  $\Phi$ , the fermions, the photon, and gluons.  $m_i$  are the field-dependent masses, and  $n_i$  is the number of degrees of freedom for species  $i$ . The function  $J_b$  ( $J_f$ ) is defined for bosons (fermions) and has well-known high- $T$  and low- $T$  expansions [86]. Write  $x^2 \equiv \frac{m_i^2}{T^2}$ , then for  $x^2 \ll 1$ ,

$$J_f(x^2) \approx -\frac{7\pi^4}{360} + \frac{\pi^2}{24}x^2 \quad (3.4)$$

$$J_b(x^2) \approx -\frac{\pi^4}{45} + \frac{\pi^2}{12}x^2 - \frac{\pi}{6}(x^2)^{3/2}. \quad (3.5)$$

The  $x^2$ -dependent term in  $J_{b/f}$  leads to symmetry-restoration at high- $T$ . For  $x^2 \gg 1$ , both fermions and bosons have the same expansion with an exponential suppression due to the Boltzmann factor [86],

$$J_{b/f}(x^2) \approx -\exp\left(-x^2\right) \left(\frac{\pi}{2}x^2\right)^{1/2}. \quad (3.6)$$

DWs are formed at temperatures below the parity-breaking scale  $v_0$ , i.e.  $T \lesssim v_0$ . The network exists for a temperature range  $T_{\text{ann}} \lesssim T \lesssim v_0$ , where  $T_{\text{ann}}$  is the DW annihilation temperature (Section IV). The DWs of DLRSM are topologically stable even after electroweak symmetry breaking (EWSB) and can survive right till the epoch of Big Bang nucleosynthesis (BBN). The evolution of the DW network before and after EWSB should therefore be considered separately.

- **Before EWSB:** When  $v_{\text{SM}} \ll T \lesssim v_0$ , we can set the  $vevs$   $\kappa_1 = \kappa_2 = 0$  as the EW symmetry is restored. On the other hand, the contribution of the ‘heavy’ fields to the one-loop temperature corrections is Boltzmann-suppressed according to eq. (3.6). So the effective potential in terms of the background fields  $v_L$  and  $v_R$  is given by,

$$\begin{aligned} V_{\text{eff}}(v_L, v_R) &= V_\chi(v_L, v_R) \\ &= -\frac{\mu_3^2}{2}(v_L^2 + v_R^2) + \frac{\rho_1}{4}(v_L^4 + v_R^4) + \frac{\rho_2}{4}v_L^2v_R^2. \end{aligned} \quad (3.7)$$

The minima and saddle points of  $V_\chi$  are given in eq. (3.10) and eq. (3.11) respectively.

---

<sup>1</sup>  $W_L^\pm$  and  $Z_L$  are taken as heavy fields since  $v_L$  can take large values in some domains.

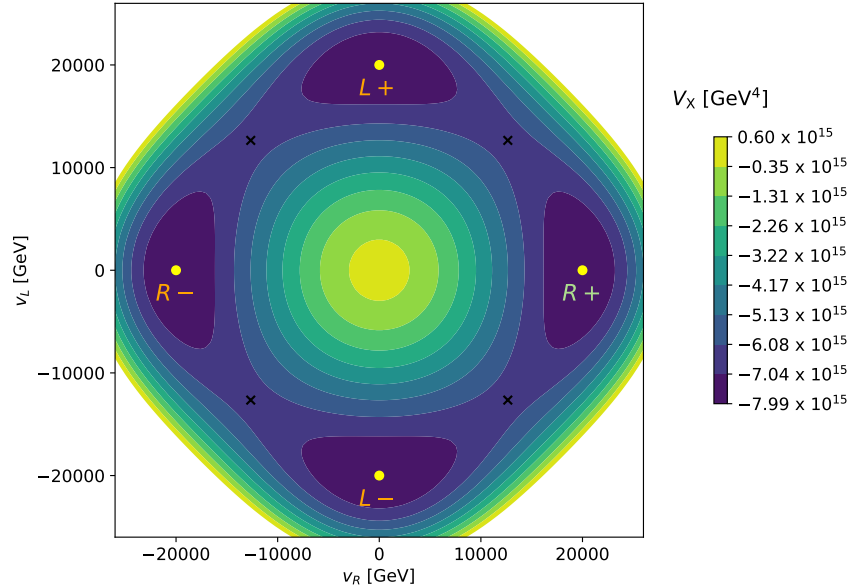


FIG. 1. The potential  $V_\chi$  for  $v_0 = 20$  TeV,  $\rho_1 = 0.2$ , and  $\rho_2 = 0.6$ . Yellow dots indicate the minima, while black crosses show the saddle points. The minimum,  $R+$ , shown in green, is consistent with the observed phenomenology.

- **After EWSB:** When  $T_{\text{ann}} \lesssim T \lesssim v_{\text{SM}}$ , the bidoublet acquires a non-zero  $vev$ . In this regime, the thermal contributions of  $v_0$ -scale fields as well as EW-scale fields are Boltzmann-suppressed. The effective potential is modified as

$$\begin{aligned} V_{\text{eff}}(v_L, v_R) &= V_\chi(v_L, v_R) + V_{\chi\Phi}(v_L, v_R; \kappa_1, \kappa_2) \\ &= c_1(v_L^2 + v_R^2) + c_2(v_L^4 + v_R^4) + c_3 v_L^2 v_R^2 + c_4 v_L v_R. \end{aligned} \quad (3.8)$$

The  $V_\Phi$  term has been dropped since it is independent of  $v_L$  and  $v_R$ . The coefficients,  $c_1, c_2, c_3, c_4$ , are given by,

$$\begin{aligned} c_1 &= -\frac{\mu_3^2}{2} + \frac{1}{4}[\kappa_1^2(\alpha_1 + \alpha_4) + \kappa_2^2(\alpha_1 + \alpha_3) + 2\kappa_1\kappa_2\alpha_2], \quad c_2 = \frac{\rho_1}{4}, \\ c_3 &= \frac{\rho_2}{4}, \quad c_4 = \frac{1}{\sqrt{2}}(\kappa_2\mu_4 + \kappa_1\mu_5). \end{aligned}$$

Non-zero values of  $\kappa_1$  and  $\kappa_2$  slightly change the positions of the minima of the effective potential. We verified that the contribution of  $V_{\chi\Phi}$  to the effective potential is numerically insignificant in the parameter space of interest, since  $\kappa_1, \kappa_2 \ll v_0$ .

Hence, the DW structure is primarily governed by  $V_\chi$ , given in eq. (3.7). In polar coordinates,  $v_R = v \cos \theta$ ,  $v_L = v \sin \theta$ , eq. (3.7) becomes,

$$V_\chi(v, \theta) = -\frac{\mu_3^2}{2}v^2 + \frac{v^4}{4}\left(\rho_1 + \frac{\rho_{21}}{2}\sin^2 2\theta\right), \quad (3.9)$$

where  $\rho_{21} = \rho_2/2 - \rho_1$ . For  $\mu_3^2 > 0$ ,  $\rho_{21} > 0$ , there are four degenerate minima,

$$(v, \theta) = \left( v_0, \frac{n\pi}{2} \right), \quad (3.10)$$

and four saddle points,

$$(v, \theta) = \left( v_1, \frac{(2n+1)\pi}{4} \right), \quad (3.11)$$

where  $n = 0, 1, 2, 3$ , and

$$v_0 = \sqrt{\frac{\mu_3^2}{\rho_1}}, \text{ and } v_1 = \sqrt{\frac{\mu_3^2}{\rho_1 + \frac{\rho_{21}}{2}}}. \quad (3.12)$$

A contour plot of  $V_\chi$  is shown in Fig. 1 for a fixed set of parameters. The potential has a  $Z_4 \simeq \mathcal{P} \times Z_2$  symmetry, with the adjacent minima connected by  $\mathcal{P}$ , and non-adjacent minima connected by  $Z_2$ . We denote the four minima  $(v_R, v_L)$  as:  $R+ \equiv (v_0, 0)$ ,  $L+ \equiv (0, v_0)$ ,  $R- \equiv (-v_0, 0)$ ,  $L- \equiv (0, -v_0)$ . The desired vacuum consistent with phenomenology is the  $R+$  vacuum<sup>2</sup>. After the  $\mathcal{P}$ -breaking PT, spatial points separated by distances larger than the correlation length  $\xi$  fall into any of the four minima with equal probability. This creates a network of domain walls separating regions of distinct vacua, each with volume  $\sim \xi^3$ . Past papers on DWs from LRSM have mostly discussed DWs that separate the  $L$ -type regions from the  $R$ -type regions. However, due to the  $Z_4$  symmetry, two kinds of DWs are formed:

1.  $LR$  DWs, denoted by  $\boxed{L \pm | R \pm}$ , which separate adjacent minima, i.e., the  $L \pm$  regions from the  $R \pm$  regions.
2.  $Z_2$  DWs, denoted by  $\boxed{L + | L -}$  or  $\boxed{R + | R -}$ , separating non-adjacent minima, i.e. the  $L(R)+$  regions from the  $L(R)-$  regions.

We will later discuss that the  $Z_2$  DWs are unstable and decay into pairs of  $LR$  DWs. The energy density  $\mathcal{E}$  of the DW network is given by the ‘00’ component of the energy-momentum tensor. For a single DW configuration perpendicular to the  $x$ -axis, separating two vacua at  $x \rightarrow \pm\infty$ ,

$$\mathcal{E} = \frac{1}{2} \left( \frac{dv_L}{dx} \right)^2 + \frac{1}{2} \left( \frac{dv_R}{dx} \right)^2 + V(v_L, v_R) + C, \quad (3.13)$$

where  $C$  is a constant chosen so that  $\mathcal{E}$  vanishes at infinity.

Due to translational symmetry, we can choose the DW profile to be centered at  $x = 0$ . Integrating  $\mathcal{E}$  along the  $x$  direction yields the energy per unit area or the DW surface tension,  $\sigma$ ,

$$\sigma = \int_{-\infty}^{\infty} \mathcal{E} dx. \quad (3.14)$$

The kink solution interpolating between the two vacua minimizes  $\sigma$ , and therefore obeys,

$$\frac{d}{dx} \left( \frac{\partial \mathcal{E}}{\partial (dv_i/dx)} \right) - \frac{\partial \mathcal{E}}{\partial v_i} = 0, \quad i \in \{L, R\}. \quad (3.15)$$

<sup>2</sup> The + or - here is just a convention. We could also take  $R-$  as the desired vacuum.

We get a pair of coupled ordinary differential equations,

$$\frac{\partial^2 v_L}{\partial x^2} = -\mu_3^2 v_L + \rho_1 v_L^3 + \frac{\rho_2}{2} v_L v_R^2, \quad (3.16)$$

$$\frac{\partial^2 v_R}{\partial x^2} = -\mu_3^2 v_R + \rho_1 v_R^3 + \frac{\rho_2}{2} v_L^2 v_R, \quad (3.17)$$

which can be solved numerically using relaxation methods (see for example refs. [87, 88]), with appropriate boundary conditions. To construct DW profiles, it is sufficient to consider  $L + |R+$  and  $R - |R+$ . The boundary conditions are:

**Case I:  $LR$  DWs**

$$\lim_{x \rightarrow -\infty} (v_R, v_L) = (0, v_0), \quad \lim_{x \rightarrow +\infty} (v_R, v_L) = (v_0, 0). \quad (3.18)$$

**Case II:  $Z_2$  DWs**

$$\lim_{x \rightarrow -\infty} (v_R, v_L) = (-v_0, 0), \quad \lim_{x \rightarrow +\infty} (v_R, v_L) = (v_0, 0). \quad (3.19)$$

It is convenient to express the equations in terms of dimensionless quantities,

$$\hat{v}_L = \frac{v_L}{v_0}, \quad \hat{v}_R = \frac{v_R}{v_0}, \quad \hat{\mu}_3^2 = \frac{\mu_3^2}{v_0^2} = \rho_1, \quad \hat{x} = x v_0, \quad (3.20)$$

where the hatted variables are dimensionless. Similarly, we can define the dimensionless surface tension,

$$\hat{\sigma} = \frac{\sigma}{v_0^3} = \int_{-\infty}^{\infty} \hat{\mathcal{E}} d\hat{x}, \quad (3.21)$$

with  $\hat{\mathcal{E}} = \frac{\mathcal{E}}{v_0^4}$  as the dimensionless energy density. We describe the procedure to obtain kink solutions in Appendix A.

In Fig. 2 we show the DW profiles for  $LR$  and  $Z_2$  cases. For the chosen benchmark,

$$\hat{\sigma}_{LR} = 0.1363, \quad \hat{\sigma}_{Z_2} = 0.4216 \implies \frac{\hat{\sigma}_{Z_2}}{\hat{\sigma}_{LR}} \approx 3.1.$$

The energy density of the two kinds of DWs differs significantly, as seen in the lower left panel. In field space, the  $LR$  DW passes through one of the saddle points, while the  $Z_2$  DW passes through the origin. Due to the greater energy density,  $Z_2$  DWs are unstable and decay into  $LR$  DWs, as discussed in Ref. [89]. By adding a small shift to the initial guess of the  $Z_2$  DW along the  $v_L$  direction we checked that the  $Z_2$  DW solution converges into a hybrid structure of two  $LR$  DWs.

Fig. 3 shows the dependence of  $\hat{\sigma}$  on the quartic couplings  $\{\rho_1, \rho_2\}$ , for  $LR$  and  $Z_2$  DWs. The surface tension of  $LR$  DWs is higher for larger values of  $\rho_1$  and  $\rho_2$ , while it is almost independent of  $\rho_2$  for  $Z_2$  DWs. In both cases, the overall dependence on  $\rho_1$  and  $\rho_2$  is weak, since the variation in  $\hat{\sigma}$  in the  $\rho_1 - \rho_2$  plane is within an order of magnitude.  $Z_2$  DWs have greater energy density than  $LR$  DWs in the entire  $\rho_1 - \rho_2$  plane. When  $\hat{\sigma}_{Z_2} > 2\hat{\sigma}_{LR}$ , a  $Z_2$



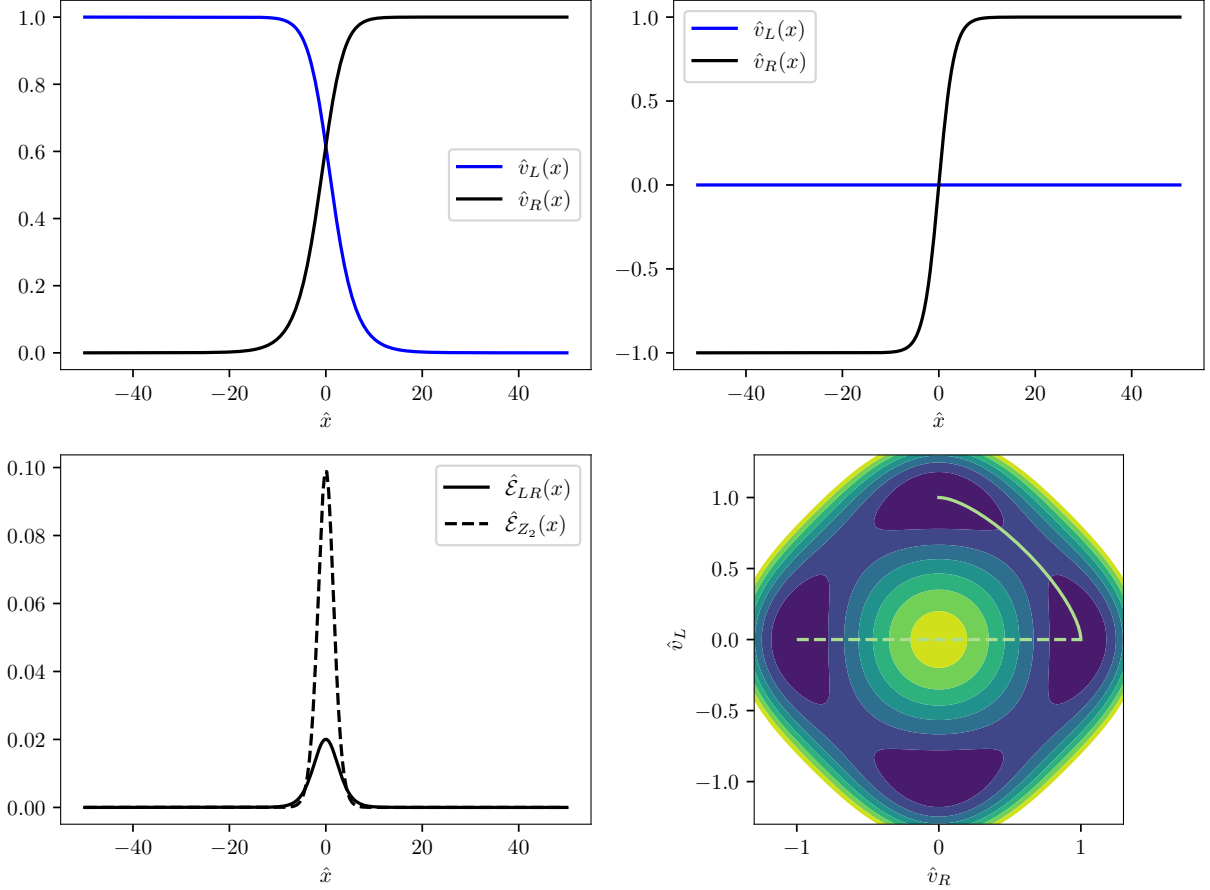


FIG. 2.  $LR$  (top-left panel) and  $Z_2$  (top-right panel) DW profiles, for  $\rho_1 = 0.2$ , and  $\rho_2 = 0.6$ . The dimensionless energy density of the DWs is shown in the bottom-left panel. The bottom-right panel shows the  $LR$  (solid line) and  $Z_2$  (dashed line) DW profiles in field space.

DW can split into two  $LR$  DWs of equal area connecting adjacent minima [89]. On the other hand if  $\hat{\sigma}_{Z_2} < 2\hat{\sigma}_{LR}$ , then a  $Z_2$  wall can split into two  $LR$  DWs of smaller surface area. The most stable configuration of the DW network consists only of  $LR$  DWs after the  $Z_2$  DWs have decayed away, as depicted in the right panel of Fig. 4. This explains why it is enough to focus on  $LR$  DWs. This discussion applies equally to TLRSM, where the potential also obeys a  $Z_4$  symmetry and has a similar vacuum structure.

#### IV. GRAVITATIONAL WAVES FROM DOMAIN WALLS

Once formed, the DWs quickly reach a scaling regime in the absence of friction, with  $\mathcal{O}(1)$  DWs per Hubble volume moving at relativistic speeds. The energy density in the scaling regime is given by [90],

$$\rho_{\text{DW}} = \mathcal{A}\sigma H, \quad (4.1)$$

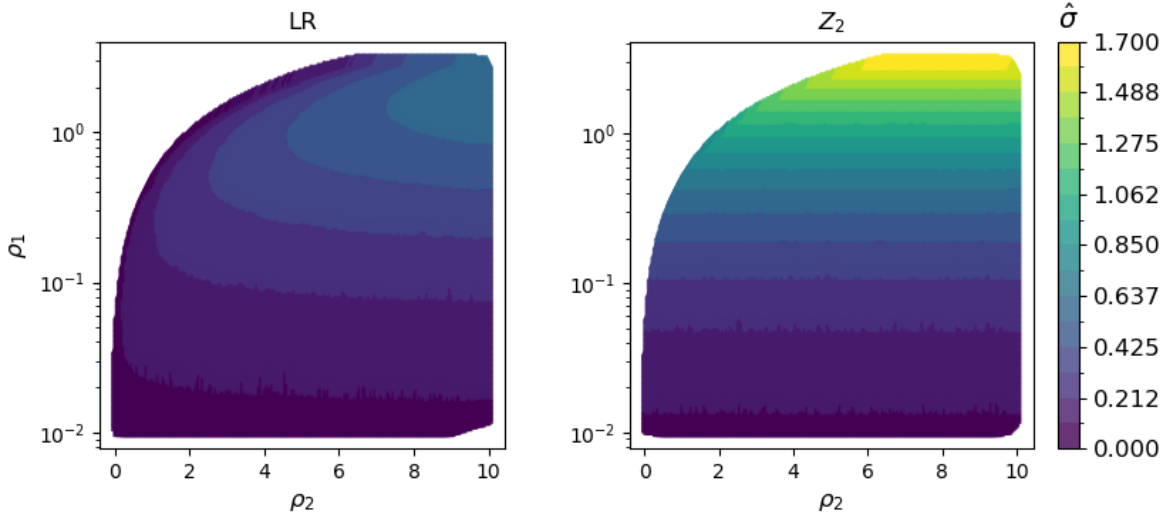


FIG. 3. Parametric dependence of  $\hat{\sigma}$  on  $\rho_1$  and  $\rho_2$  for  $LR$  (left panel) and  $Z_2$  (right panel) DWs. The surface tension of  $Z_2$  DWs is greater than that of  $LR$  DWs.

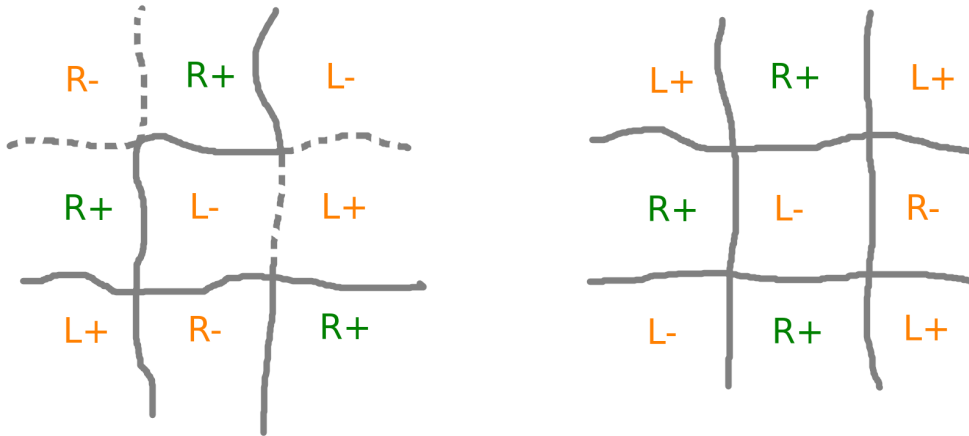


FIG. 4. Left: Schematic diagram of a typical DW network showing  $LR$  (solid line) and  $Z_2$  (dashed line) DWs. Right: In the stable configuration, the  $Z_2$  DWs are absent and the network consists entirely of  $LR$  DWs. The vacuum consistent with phenomenology,  $R+$ , is shown in green, while the rest are shown in orange.

where  $\mathcal{A} \sim 0.8$  is a numerical factor obtained from simulations and  $H$  is the Hubble parameter.

At time  $t$ ,  $\rho_{\text{DW}} \propto H(t) \propto 1/t$ , while the energy density of matter and radiation falls faster, implying that DWs dominate the energy density of the universe at late times. By introducing a small bias term in the potential,  $V_{\text{bias}}$ , via explicit  $\mathcal{P}$ -breaking operators, we can lift the degeneracy of the four vacua in such a way that the  $R+$  vacuum is favored. This creates a pressure difference across the DWs, causing the domains with the preferred vacuum

to grow in size. Due to the bias, the DWs eventually begin to annihilate at a temperature  $T_{\text{ann}}$ , defined by the condition,  $\rho_{\text{DW}}(T_{\text{ann}}) \sim V_{\text{bias}}$ . Assuming radiation-domination [35],

$$T_{\text{ann}} \simeq \frac{5 \text{ MeV}}{\sqrt{\mathcal{A}}} \left( \frac{10.75}{g_*(T_{\text{ann}})} \right)^{\frac{1}{4}} \left( \frac{V_{\text{bias}}^{1/4}}{10 \text{ MeV}} \right)^2 \left( \frac{10^5 \text{ GeV}}{\sigma^{1/3}} \right)^{\frac{3}{2}}. \quad (4.2)$$

where  $g_*(T_{\text{ann}})$  is the number of relativistic degrees of freedom at  $T_{\text{ann}}$ . To accommodate cosmological constraints, DWs must annihilate before the BBN epoch, i.e.  $T_{\text{ann}} > T_{\text{BBN}} \sim 1 \text{ MeV}$ . This yields a lower bound on  $V_{\text{bias}}$ ,

$$V_{\text{bias}} > \frac{\mathcal{A}}{25} (10 \text{ MeV})^4 \left( \frac{\sigma^{1/3}}{10^5 \text{ GeV}} \right)^3. \quad (4.3)$$

Similarly, an upper bound on  $V_{\text{bias}}$  is obtained by requiring that domains of the preferred vacuum must not percolate [90],

$$\frac{V_{\text{bias}}}{V_0} > \ln \left( \frac{1 - p_c}{p_c} \right), \quad (4.4)$$

where  $p_c = 0.311$  is the critical value above which the favored vacuum percolates and  $V_0$  is the height of the barrier separating the minima. For *LR* DWs,

$$V_0 = \frac{1}{4} v_0^4 \left( \frac{\rho_2 - 2\rho_1}{\rho_2 + 2\rho_1} \right) \approx \frac{1}{4} v_0^4, \quad (4.5)$$

where the last approximation holds when  $\rho_2 \gg \rho_1$ . The condition of eq. (4.4) is easily satisfied since we are interested in  $V_{\text{bias}} \ll v_0^4$ .

The bias term can be generated by introducing operators that explicitly break the  $\mathcal{P}$  symmetry. Since quantum gravity effects destroy global symmetries, Planck scale-suppressed higher dimensional operators provide an elegant way to generate the bias term. Indeed, this possibility has been considered in the literature [40, 77, 91, 92]. In this paper, we do not assume any particular origin of the bias term and keep  $V_{\text{bias}}$  as a free parameter.

A dimensionless parameter,  $\alpha_*$ , captures the DW energy density at annihilation,

$$\begin{aligned} \alpha_* &= \frac{\rho_{\text{DW}}(T_{\text{ann}})}{\rho_{\text{rad}}(T_{\text{ann}})}, \\ \rho_{\text{rad}}(T) &= \frac{\pi^2}{30} g_*(T) T^4, \end{aligned} \quad (4.6)$$

Using eq. (4.1), we get [35],

$$\alpha_* \simeq \mathcal{A} \sqrt{\frac{g_*(T_{\text{ann}})}{10.75}} \left( \frac{\sigma^{1/3}}{10^5 \text{ GeV}} \right)^3 \left( \frac{10 \text{ MeV}}{T_{\text{ann}}} \right)^2. \quad (4.7)$$

We consider the scenario where the DWs decay into standard model particles, in which case, BBN restricts  $T_{\text{ann}} \gtrsim 2.7 \text{ MeV}$  [93, 94]. We also impose  $\alpha_* < 0.3$  to ensure no deviation from radiation domination [35].

The relic GW spectrum is defined as,

$$h^2\Omega_{\text{GW}} = \frac{h^2}{\rho_c} \frac{\partial \rho_{\text{GW}}}{\partial \ln f}, \quad (4.8)$$

where  $\rho_c$  is the critical density, given by

$$\rho_c = \frac{3H_0^2}{8\pi G}, \quad (4.9)$$

and  $H_0 = 100 h \text{ km s}^{-1} \text{ Mpc}^{-1}$  is the present-day Hubble constant with  $h = 0.6736 \pm 0.0054$  [95], and  $G$  is Newton's gravitational constant.

GWs are produced due to DW surface oscillations [96–98], with dominant emission happening at  $T = T_{\text{ann}}$ . Assuming all the GWs are produced at  $T_{\text{ann}}$ , the GW spectrum is given by [35, 99],

$$h^2\Omega_{\text{GW}}^{\text{DW}}(f) \simeq 10^{-10} \tilde{\epsilon}_{\text{GW}} \left( \frac{10.75}{g_*(T_{\text{ann}})} \right)^{\frac{1}{3}} \left( \frac{\alpha_*}{0.01} \right)^2 S \left( \frac{f}{f_p^0} \right), \quad (4.10)$$

where  $\tilde{\epsilon}_{\text{GW}} = 0.7 \pm 0.4$ . The peak frequency  $f_p^0$  is given by,

$$f_p^0 \simeq 10^{-9} \text{ Hz} \left( \frac{g_*(T_{\text{ann}})}{10.75} \right)^{\frac{1}{6}} \left( \frac{T_{\text{ann}}}{10 \text{ MeV}} \right), \quad (4.11)$$

and the shape function of the GW spectrum  $S$  has the form,

$$S(x) = \frac{(\gamma + \beta)^\delta}{(\beta x^{-\frac{\gamma}{\delta}} + \gamma x^{\frac{\beta}{\delta}})^\delta}. \quad (4.12)$$

We set  $\gamma = 3$  from causality [56], while numerical analyses determine  $\delta, \beta \simeq 1$ . Following [99], we set  $\delta, \beta = 1$ . Note that,

$$h^2\Omega_{\text{GW}}^{\text{DW}}(f_p^0) \propto \alpha_*^2 \propto \frac{\sigma^2}{V_{\text{bias}}} \propto \frac{v_0^6}{V_{\text{bias}}},$$

indicating a strong dependence of the amplitude on the scale  $v_0$ .

After the annihilation of DWs, the GW production stops, and  $\rho_{\text{GW}}$  redshifts like SM radiation, contributing to the number of relativistic degrees of freedom,  $g_*(T)$ . Around BBN temperatures,  $T \simeq \mathcal{O}(\text{MeV})$ , this extra contribution from GWs can be restricted by considering the limits on  $\Delta N_{\text{eff}}$  from CMB and BBN, where  $\Delta N_{\text{eff}} = N_\nu - 3$ , and  $N_\nu$  is the effective number of light neutrino species at BBN. The upper bound on the GW amplitude is [100, 101],

$$h^2\Omega_{\text{GW}} \lesssim 5.6 \times 10^{-6} \Delta N_{\text{eff}}. \quad (4.13)$$

The existing limit on  $\Delta N_{\text{eff}}$  from Planck is,  $\Delta N_{\text{eff}} \lesssim 0.28$  at 95% confidence level. Upcoming CMB experiments will be able to probe smaller values of  $\Delta N_{\text{eff}}$  [95].

## V. RESULTS

### A. MCMC analysis

We use the NG15 data to carry out the Bayesian analysis. Given PTA data  $\mathcal{D}$ , a hypothesis  $\mathcal{H}$ , and parameters  $\Theta$ , we use the posterior distribution  $P(\Theta|\mathcal{D}, \mathcal{H})$ , reconstructed from MCMC analysis, to identify best-fit parameter ranges and set upper limits on them. We consider two hypotheses: (i)  $\mathcal{H}_1$ : the DLRSW DW model assuming the SMBH background is negligible, and (ii)  $\mathcal{H}_2$ : the DLRSW DW+SMBHB model, where the GW contribution from DLRSW DWs is combined with the contribution from SMBHBs. The DLRSW parameters of interest are,

$$\Theta_1 \equiv \{v_0, \rho_1, \rho_2, V_{\text{bias}}\}.$$

For  $\mathcal{H}_1$ , we first obtain the functional dependence of  $\hat{\sigma}(\rho_1, \rho_2)$  by interpolating the numerical values shown in Fig. 3, so that the surface tension is obtained as,  $\sigma(v_0, \rho_1, \rho_2) = \hat{\sigma}(\rho_1, \rho_2)v_0^3$ . Next, we calculate  $T_{\text{ann}}$  according to eq. (4.2), while  $\alpha_*$  is calculated using eq. (4.7). The constraints  $T_{\text{ann}} \gtrsim 2.7 \text{ MeV}$  and  $\alpha_* < 0.3$ , are imposed as discussed in the previous section. Thus we obtain the GW spectrum in terms of DLRSW parameters

$$\mathcal{H}_1 : \quad h^2\Omega_{\text{GW}}^{\text{DW}}(f; v_0, \rho_1, \rho_2, V_{\text{bias}}).$$

For  $\mathcal{H}_2$ , we superimpose the contribution of SMBHBs with the DLRSW DW contribution. For low frequencies,  $f \ll 1 \text{ year}^{-1}$ , the SMBHB spectrum is given by a simple power law [102–106],

$$h^2\Omega_{\text{GW}}^{\text{BHB}}(f) = \frac{2\pi^2 h^2 A_{\text{BHB}}^2}{3H_0^2} \left(\frac{f}{f_{\text{yr}}}\right)^{5-\gamma_{\text{BHB}}} f_{\text{yr}}^2, \quad (5.1)$$

where  $f_{\text{yr}} = 1 \text{ year}^{-1} = 3.17 \times 10^{-8} \text{ Hz}$ . The spectrum falls off rapidly at larger frequencies,  $f \gg 1 \text{ year}^{-1}$ . If the orbital evolution of the binaries is purely driven by GW emission, the parameter  $\gamma_{\text{BHB}}$  takes the value,  $\gamma_{\text{BHB}} = 13/3$ . To account for environmental effects  $\gamma_{\text{BHB}}$  is taken as a free parameter, along with  $A_{\text{BHB}}$ , so that the parameter set is,

$$\Theta_2 \equiv \{v_0, \rho_1, \rho_2, V_{\text{bias}}, A_{\text{BHB}}, \gamma_{\text{BHB}}\}.$$

The GW signal is hypothesised as,

$$\mathcal{H}_2 : \quad h^2\Omega_{\text{GW}}^{\text{DW}}(f; v_0, \rho_1, \rho_2, V_{\text{bias}}) + h^2\Omega_{\text{GW}}^{\text{BHB}}(f; A_{\text{BHB}}, \gamma_{\text{BHB}}).$$

The Bayesian analysis is implemented using the PTArcade package [107, 108], which is a wrapper for the ENTERPRISE code [109], and incorporates PTA data. For the DLRSW DW model, we sample the parameters  $v_0$ ,  $V_{\text{bias}}$  and  $\rho_1$  from a log-uniform distribution, and  $\rho_2$  from a uniform distribution. The parameter ranges for the priors are given in the second column of Table I. The SMBHB parameters ( $\log_{10} A_{\text{BHB}}, \gamma_{\text{BHB}}$ ) are sampled from a normal bivariate distribution taken from Ref. [56].

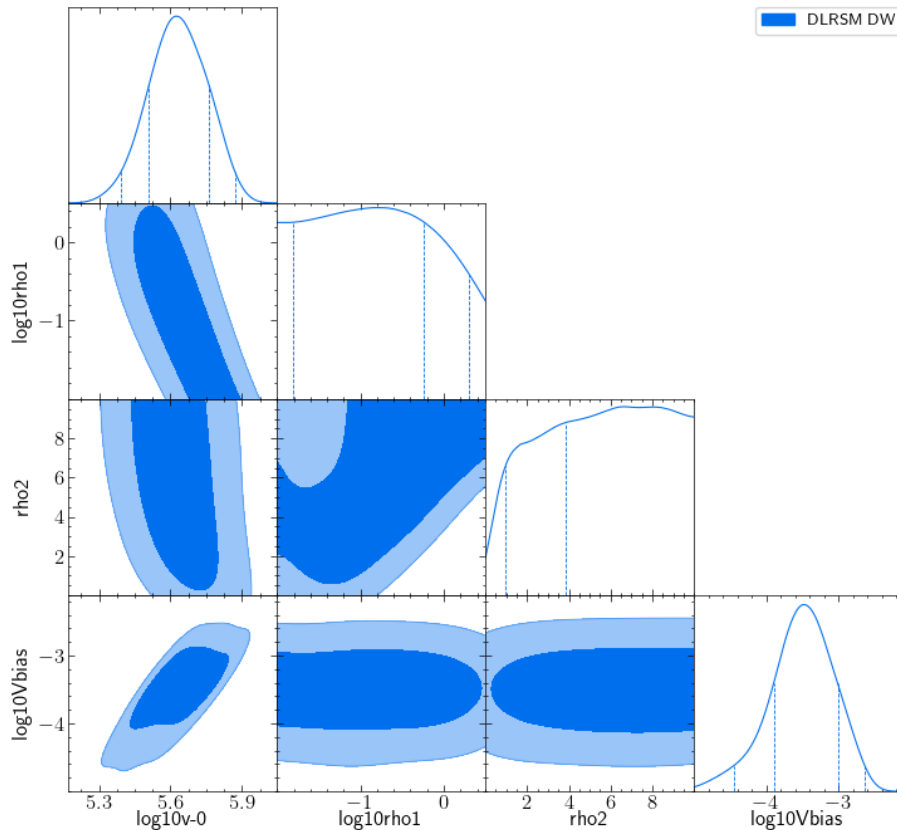


FIG. 5. The posterior probability distribution of the DLRSM DW fit to the NG15 data.

The posteriors for DLRSM DWs are shown in Fig. 5. The  $\mathcal{P}$ -breaking scale  $v_0$  and the bias term  $V_{\text{bias}}$  are constrained in a narrow range, as indicated by the closed contours for the 68% and 95% credible intervals. On the other hand, there is a weak dependence on the quartic couplings  $\rho_1$  and  $\rho_2$ . Note also that  $\rho_1 \ll \rho_2$  in the 68% and 95% credible regions. A positive correlation is observed between  $v_0$  and  $V_{\text{bias}}$ , which is because, for a given scale  $v_0$ , we can always find an appropriate value of  $V_{\text{bias}}$ , which best explains the data. In Fig. 6, we show the posterior distribution for the DLRSM DW+SMBHB model, with the labels gw-bhb-0 and gw-bhb-1 denoting the SMBHB parameters  $\log_{10} A_{\text{BHB}}$  and  $\gamma_{\text{BHB}}$  respectively. The DLRSM parameters follow a similar distribution as in the previous case, and the other two parameters take the maximum posterior values  $(\log_{10} A_{\text{BHB}}, \gamma_{\text{BHB}}) = (-15.44, 4.69)$ . The predicted spectral index,  $\gamma_{\text{BHB}} = 13/3$ , lies just outside the 68% credible interval. The likelihood ratio of the DLRSM DW relative to the the DLRSM DW+SMBHB model corresponds to,  $-2\Delta \ln l_{\text{max}} = -1.2$ , indicating that the pure DLRSM DW model is slightly favored.

Table I summarizes the prior ranges, maximum posteriors, and 68% credible intervals for all the parameters in the two scenarios. In particular, the maximum posterior values of  $v_0$

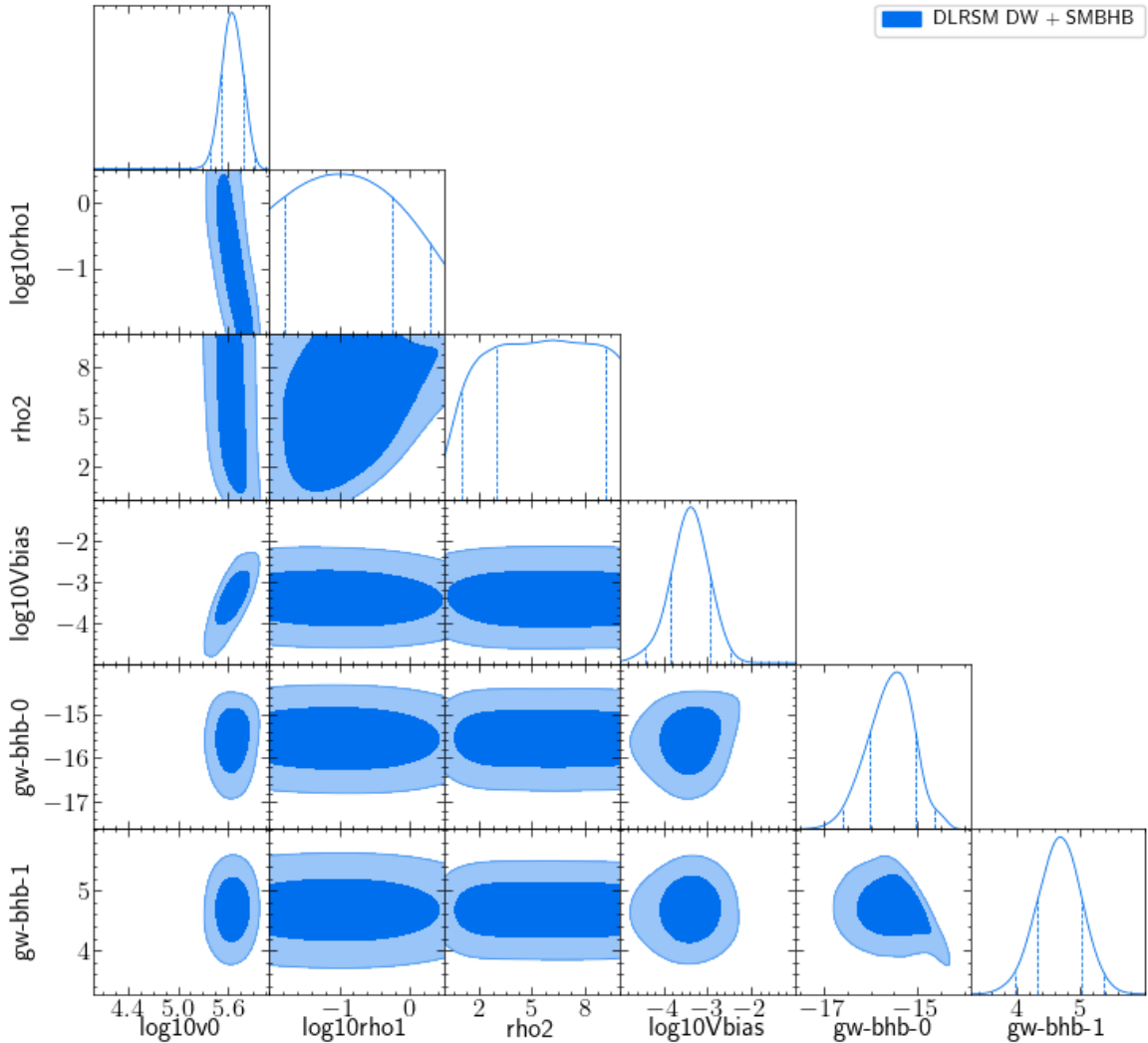


FIG. 6. Same as fig. 5, but also including the contribution from SMBHB.

and  $V_{\text{bias}}$  for DLRSM DW model are,

$$v_0 = 4.36 \times 10^5 \text{ GeV}, \quad V_{\text{bias}} = 3.31 \times 10^{-4} \text{ GeV}^4. \quad (5.2)$$

## B. Detection prospects

We now discuss the prospects of detecting the GW signal using the best-fit parameter values at upcoming GW observatories. In Fig. 7 we show the median GW spectra fitted to the NG15 data along with  $1\sigma$  and  $2\sigma$  confidence intervals, for the DLRSM DW model (left panel), and DLRSM DW combined with SMBHB (right panel). The green violins correspond to the posterior distribution of  $\Omega_{\text{GW}}$  in 14 frequency bins, predicted by the NG15 data [1].

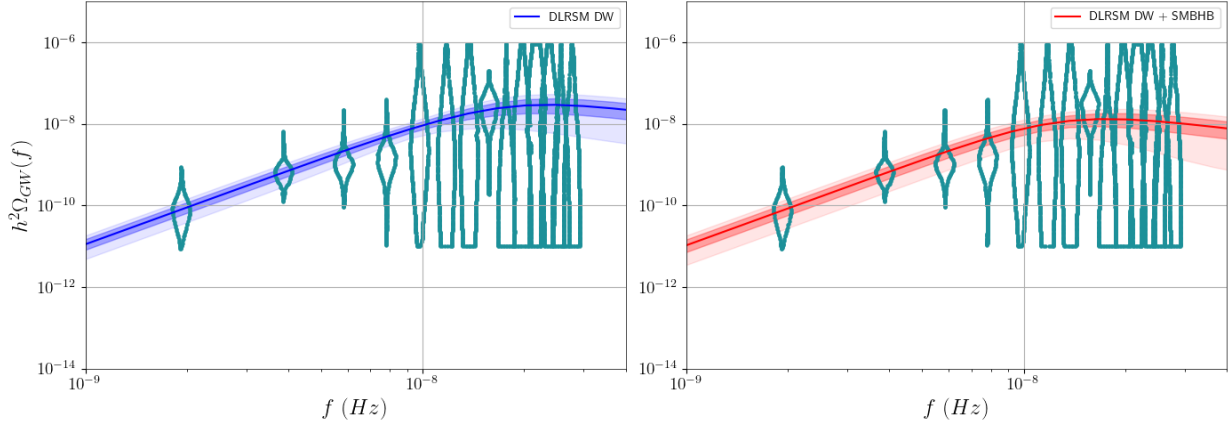


FIG. 7. Median GW spectra for DLRSM DWs, along with their 68% and 95% posterior envelopes.

Parameter	Uniform prior range	Maximum Posterior		68% credible interval	
		$\mathcal{H}_1$	$\mathcal{H}_2$	$\mathcal{H}_1$	$\mathcal{H}_2$
$\log_{10} v_0/\text{GeV}$	[4, 8]	5.63	5.66	[5.52, 5.77]	[5.52, 5.79]
$\log_{10} V_{\text{bias}}/\text{GeV}^4$	[-5, -1]	-3.47	-3.37	[-3.90, -3.05]	[-3.82, -2.91]
$\log_{10} \rho_1$	[-2.5, 0.5]	-0.77	-1.00	[-1.90, -0.35]	[-1.76, -0.23]
$\rho_2$	[0, 10]	6.55	6.50	[2.88, 9.16]	[3.03, 9.23]
$\log_{10} A_{\text{BHB}}$	-	-	-15.44	-	[-15.97, -15.02]
$\gamma_{\text{BHB}}$	-	-	4.69	-	[4.35, 5.04]

TABLE I. Priors, along with the maximum posterior values and 68% credible intervals for the parameters, for the two hypotheses considered.

With more data, the posteriors would narrow down, enabling a more precise parameter estimation in the future.

Fig. 8 shows the median GW spectra for the two models for a wider range of frequencies, with the power-law integrated sensitivity curves (PLISCs) [110] of upcoming GW detectors, SKA [111],  $\mu\text{Ares}$  [112], LISA [113], BBO [114], FP-DECIGO [115], CE [116], and ET [117]. The shaded grey region shows the region excluded by the  $\Delta N_{\text{eff}}$  bound coming from Planck data. Except  $\mu\text{Ares}$ , the PLISCs of all upcoming detectors are taken from Ref. [118], using the threshold signal-to-noise ratio (SNR) of 1, and time of observation,  $\tau = 1$  year, while  $\tau = 20$  years for SKA. The PLISC for  $\mu\text{Ares}$  is calculated for threshold SNR of 10, and  $\tau = 7$  years. If the GW spectrum results from the DLRSM DW model, considered with or without SMBHBs, it would be observed by future observatories, particularly  $\mu\text{Ares}$ , LISA,



FP-DECIGO, and BBO, with a high SNR. The signal will also be confirmed by upcoming PTAs such as SKA. If the  $\mathcal{P}$ -breaking PT is first-order, one would observe a double-peaked GW spectrum, with the additional higher frequency peak coming from FOPT, as discussed in Ref. [85]. For  $v_0 \gtrsim 10^5$  GeV, the peak from FOPT would be detected by CE and ET.

In DLRSM, the extra heavy degrees of freedom including neutral  $CP$ -even scalars  $H_{1,2,3}$ ,  $CP$ -odd scalars  $A_{1,2}$ , charged scalars  $H_{1,2}^\pm$  and gauge bosons  $Z_2, W_2^\pm$ , all have  $\mathcal{O}(v_0)$  masses. Due to the high parity-breaking scale favored by the NG15,  $v_0 \gtrsim 10^5$  GeV, the prospects of detecting these heavy particles at upcoming collider experiments are weak.

## VI. DISCUSSION

After the 15-year NANOGrav dataset analysis reported convincing evidence of a low-frequency GW background, several works have compared the possible models to explain it. In addition to the standard interpretation of GWs produced by SMBHBs, many cosmological models have been proposed. One such model is the DW model, in which the GW background is due to a network of DWs in the early universe. The formation of DWs requires the existence of a discrete symmetry which is spontaneously broken in a phase transition. In LRSMs, the discrete parity symmetry can be elegantly incorporated to explain the parity violation observed in SM via spontaneous symmetry breaking. The parity-breaking PT in LRSM can give rise to DWs. Since LRSMs typically require the scale of parity-breaking,  $v_0$ , to be large compared to the EW scale, the DW surface tension,  $\sigma \propto v_0^3$ , can be made large enough to explain the NG15 result. In this work, we considered the DWs of the parity symmetric DLRSM as the source of the NG15 signal.

Earlier discussions on DWs in LRSM mostly focused on TLRSM and reported the scale of  $\mathcal{P}$ -breaking required to explain the PTA signal using benchmarks obtained from order of magnitude estimates. In this paper, for DLRSM, we found the explicit parameter dependence of the surface tension and carried out a Bayesian analysis to constrain model parameters. Due to the  $Z_4$  symmetry of the DLRSM potential, two kinds of DWs, i.e.  $LR$  and  $Z_2$  DWs are formed. The surface tension of the  $Z_2$  walls is higher than that of  $LR$  DWs. Earlier works on DWs in LRSM mainly focused on  $LR$  DWs and did not discuss the fate of  $Z_2$  DWs in detail. We argued that the  $Z_2$  DWs are unstable and decay into  $LR$  DWs, thus providing a rationale for considering only  $LR$  DWs. The arguments presented here can also be applied to TLRSM. The DW surface tension depends weakly on the quartic couplings  $\rho_1, \rho_2$ , and the primary dependence is on  $v_0$ . The DW network must annihilate before the epoch of BBN to respect cosmological constraints, which can be achieved via explicit parity-breaking terms in the potential, resulting in a bias,  $V_{\text{bias}}$ . While such operators can be motivated by quantum gravity and grand unified theories, we considered  $V_{\text{bias}}$  as a free parameter.

For the Bayesian analysis, we considered the case where the NG15 signal is entirely ex-

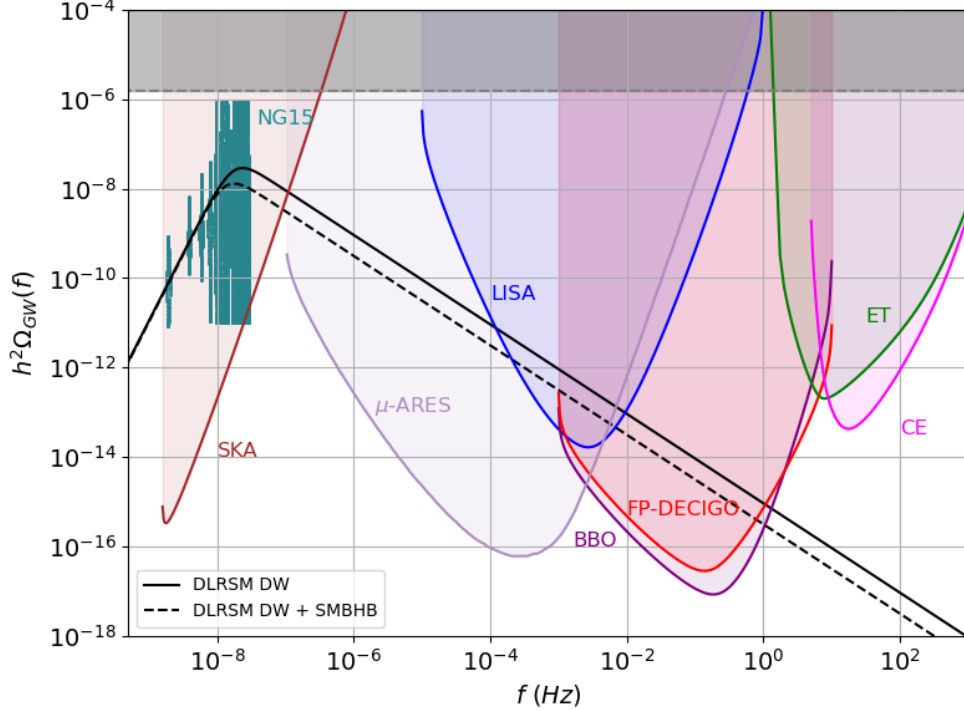


FIG. 8. Median GW spectrum for DLRSM DW (solid black) and DLRSM DWs+SMBHB model (dashed black) along with sensitivity curves for upcoming GW detectors. The shaded grey region is excluded by the Planck  $\Delta N_{\text{eff}}$  bound.

plained by DLRSM DWs and the case where the SMBHB contribution is also included. The maximum posterior values of the parameters and the 68% credible intervals are summarized in Table I. The strong dependence of the peak amplitude of the GW spectrum on  $\sigma$ , and  $V_{\text{bias}}$ , i.e.  $\Omega_{\text{GW}}^{\text{DW}}(f_{\text{peak}}) \propto \sigma^2/V_{\text{bias}}$ , results in a tight constraint on  $v_0$  and  $V_{\text{bias}}$ , as reflected by the respective 68% credible intervals. On the other hand, the quartic couplings  $\rho_1$  and  $\rho_2$  are less constrained. For the DLRSM DW+DW case, the spectral index  $\gamma_{\text{BHB}}$  lies outside the 68% credible interval, indicating a tension with the NG15 results.

The median GW spectra are presented in Fig. 7 and Fig. 8, which show a good agreement with the violins of NG15 data. If the signal is due to DWs, future GW observatories such as  $\mu\text{Ares}$ , LISA, BBO, and FP-DECIGO would also observe a GW background at higher frequencies. Moreover, if the parity-breaking PT is first-order, it would give rise to a double-peaked spectrum, with the higher frequency peak observable by ET and CE.

In this paper, we have neglected the effect of friction on the DWs from the thermal plasma, which could dampen the GW signal. Since the couplings of the fields constituting the wall with the SM fields are small, the friction is expected to be negligible. In addition, the GW spectrum from SMBHBs is modeled assuming the binaries lose their energy entirely from GW production. Since current observations numerical simulations have a large uncertainty in the spectral shape, the power-law given in eq. (5.1) serves as a reasonable approximation [56].

## VII. ACKNOWLEDGEMENTS

DR thanks Subhendu Rakshit, Siddhartha Karmakar, and Suman Majumdar for helpful discussions. This work is supported by DST, via SERB Grants no. MTR/2019/000997 and no. CRG/2019/002354.

### Appendix A: Kink solutions

The dimensionless energy density is given by,

$$\hat{\mathcal{E}} = \frac{\mathcal{E}}{v_0^4} = \frac{1}{2} \left( \frac{d\hat{v}_L}{dx} \right)^2 + \frac{1}{2} \left( \frac{d\hat{v}_R}{dx} \right)^2 + \hat{V}(\hat{v}_L, \hat{v}_R) + \hat{C}. \quad (\text{A1})$$

We can rescale eq. (3.16) and eq. (3.17) as,

$$\frac{\partial^2 \hat{v}_L}{\partial \hat{x}^2} = -\hat{\mu}_3^2 \hat{v}_L + \rho_1 \hat{v}_L^3 + \frac{\rho_2}{2} \hat{v}_L \hat{v}_R^2 \quad (\text{A2})$$

$$\frac{\partial^2 \hat{v}_R}{\partial \hat{x}^2} = -\hat{\mu}_3^2 \hat{v}_R + \rho_1 \hat{v}_R^3 + \frac{\rho_2}{2} \hat{v}_L^2 \hat{v}_R. \quad (\text{A3})$$

In relaxation methods, a fictitious ‘time’ variable,  $\hat{t}$  is introduced, and the above equations are written as,

$$\frac{\partial \hat{v}_L}{\partial \hat{t}} = \frac{\partial^2 \hat{v}_L}{\partial \hat{x}^2} + \hat{\mu}_3^2 \hat{v}_L - \rho_1 \hat{v}_L^3 - \frac{\rho_2}{2} \hat{v}_L \hat{v}_R^2 \quad (\text{A4})$$

$$\frac{\partial \hat{v}_R}{\partial \hat{t}} = \frac{\partial^2 \hat{v}_R}{\partial \hat{x}^2} + \hat{\mu}_3^2 \hat{v}_R - \rho_1 \hat{v}_R^3 - \frac{\rho_2}{2} \hat{v}_L^2 \hat{v}_R. \quad (\text{A5})$$

Eq. (A2) and eq. (A3) are recovered in the limit  $\frac{\partial}{\partial \hat{t}} \hat{v}_{L,R} \rightarrow 0$ . We discretize the spatial and temporal coordinates with step size  $\Delta \hat{x}$  and  $\Delta \hat{t}$  respectively and express the derivatives in terms of second-order finite differences. The solution converges if  $\Delta \hat{t} \leq \Delta \hat{x}^2/2$ .

For numerical purposes, we approximate spatial infinity by a value  $R = 50$  and linearly interpolate the boundary conditions eq. (3.18) and eq. (3.19), for the initial guess of  $LR$  and  $Z_2$  solutions.

- 
- [1] Gabriella Agazie et al. The NANOGrav 15 yr Data Set: Evidence for a Gravitational-wave Background. *Astrophys. J. Lett.*, 951(1):L8, 2023.
  - [2] J. Antoniadis et al. The second data release from the European Pulsar Timing Array - III. Search for gravitational wave signals. *Astron. Astrophys.*, 678:A50, 2023.
  - [3] Daniel J. Reardon et al. Search for an Isotropic Gravitational-wave Background with the Parkes Pulsar Timing Array. *Astrophys. J. Lett.*, 951(1):L6, 2023.

- [4] John Ellis, Malcolm Fairbairn, Gert Hütsi, Juhan Raidal, Juan Urrutia, Ville Vaskonen, and Hardi Veermäe. Gravitational waves from supermassive black hole binaries in light of the NANOGrav 15-year data. *Phys. Rev. D*, 109(2):L021302, 2024.
- [5] Anish Ghoshal and Alessandro Strumia. Probing the Dark Matter density with gravitational waves from super-massive binary black holes. *JCAP*, 02:054, 2024.
- [6] Zhao-Qiang Shen, Guan-Wen Yuan, Yi-Ying Wang, and Yuan-Zhu Wang. Dark Matter Spike surrounding Supermassive Black Holes Binary and the nanohertz Stochastic Gravitational Wave Background. 6 2023.
- [7] Tom Broadhurst, Chao Chen, Tao Liu, and Kai-Feng Zheng. Binary Supermassive Black Holes Orbiting Dark Matter Solitons: From the Dual AGN in UGC4211 to NanoHertz Gravitational Waves. 6 2023.
- [8] Yan-Chen Bi, Yu-Mei Wu, Zu-Cheng Chen, and Qing-Guo Huang. Implications for the supermassive black hole binaries from the NANOGrav 15-year data set. *Sci. China Phys. Mech. Astron.*, 66(12):120402, 2023.
- [9] Chao Zhang, Ning Dai, Qing Gao, Yungui Gong, Tong Jiang, and Xuchen Lu. Detecting new fundamental fields with pulsar timing arrays. *Phys. Rev. D*, 108(10):104069, 2023.
- [10] Gabriele Franciolini, Antonio Iovino, Junior., Ville Vaskonen, and Hardi Veermäe. Recent Gravitational Wave Observation by Pulsar Timing Arrays and Primordial Black Holes: The Importance of Non-Gaussianities. *Phys. Rev. Lett.*, 131(20):201401, 2023.
- [11] Sunny Vagnozzi. Inflationary interpretation of the stochastic gravitational wave background signal detected by pulsar timing array experiments. *JHEAp*, 39:81–98, 2023.
- [12] Keisuke Inomata, Kazunori Kohri, and Takahiro Terada. Detected stochastic gravitational waves and subsolar-mass primordial black holes. *Phys. Rev. D*, 109(6):063506, 2024.
- [13] Reza Ebadi, Soubhik Kumar, Amara McCune, Hanwen Tai, and Lian-Tao Wang. Gravitational waves from stochastic scalar fluctuations. *Phys. Rev. D*, 109(8):083519, 2024.
- [14] Lang Liu, Zu-Cheng Chen, and Qing-Guo Huang. Implications for the non-Gaussianity of curvature perturbation from pulsar timing arrays. *Phys. Rev. D*, 109(6):L061301, 2024.
- [15] Katsuya T. Abe and Yuichiro Tada. Translating nano-Hertz gravitational wave background into primordial perturbations taking account of the cosmological QCD phase transition. *Phys. Rev. D*, 108(10):L101304, 2023.
- [16] Caner Unal, Alexandros Papageorgiou, and Ipeei Obata. Axion-Gauge Dynamics During Inflation as the Origin of Pulsar Timing Array Signals and Primordial Black Holes. 7 2023.
- [17] Hassan Firouzjahi and Alireza Talebian. Induced gravitational waves from ultra slow-roll inflation and pulsar timing arrays observations. *JCAP*, 10:032, 2023.
- [18] Pritha Bari, Nicola Bartolo, Guillem Domènech, and Sabino Matarrese. Gravitational waves induced by scalar-tensor mixing. *Phys. Rev. D*, 109(2):023509, 2024.
- [19] Kingman Cheung, C. J. Ouseph, and Po-Yan Tseng. NANOGrav Signal and PBH from the Modified Higgs Inflation. 7 2023.

- [20] Nilanjandev Bhaumik, Rajeev Kumar Jain, and Marek Lewicki. Ultralow mass primordial black holes in the early Universe can explain the pulsar timing array signal. *Phys. Rev. D*, 108(12):123532, 2023.
- [21] Mohammad Ali Gorji, Misao Sasaki, and Teruaki Suyama. Extra-tensor-induced origin for the PTA signal: No primordial black hole production. *Phys. Lett. B*, 846:138214, 2023.
- [22] Kohei Fujikura, Sudhakantha Girmohanta, Yuichiro Nakai, and Motoo Suzuki. NANOGrav signal from a dark conformal phase transition. *Phys. Lett. B*, 846:138203, 2023.
- [23] Andrea Addazi, Yi-Fu Cai, Antonino Marciano, and Luca Visinelli. Have pulsar timing array methods detected a cosmological phase transition? *Phys. Rev. D*, 109(1):015028, 2024.
- [24] Yang Bai, Ting-Kuo Chen, and Mrunal Korwar. QCD-collapsed domain walls: QCD phase transition and gravitational wave spectroscopy. *JHEP*, 12:194, 2023.
- [25] Eugenio Megias, Germano Nardini, and Mariano Quiros. Pulsar timing array stochastic background from light Kaluza-Klein resonances. *Phys. Rev. D*, 108(9):095017, 2023.
- [26] Chengcheng Han, Ke-Pan Xie, Jin Min Yang, and Mengchao Zhang. Self-interacting dark matter implied by nano-Hertz gravitational waves. *Phys. Rev. D*, 109(11):115025, 2024.
- [27] Lei Zu, Chi Zhang, Yao-Yu Li, Yuchao Gu, Yue-Lin Sming Tsai, and Yi-Zhong Fan. Mirror QCD phase transition as the origin of the nanohertz Stochastic Gravitational-Wave Background. *Sci. Bull.*, 69:741–746, 2024.
- [28] Tathagata Ghosh, Anish Ghoshal, Huai-Ke Guo, Fazlollah Hajkarim, Stephen F. King, Kuver Sinha, Xin Wang, and Graham White. Did we hear the sound of the Universe boiling? Analysis using the full fluid velocity profiles and NANOGrav 15-year data. *JCAP*, 05:100, 2024.
- [29] Pasquale Di Bari and Moinul Hossain Rahat. The split majoron model confronts the NANOGrav signal. 7 2023.
- [30] Juan S. Cruz, Florian Niedermann, and Martin S. Sloth. NANOGrav meets Hot New Early Dark Energy and the origin of neutrino mass. *Phys. Lett. B*, 846:138202, 2023.
- [31] Yann Gouttenoire. First-Order Phase Transition Interpretation of Pulsar Timing Array Signal Is Consistent with Solar-Mass Black Holes. *Phys. Rev. Lett.*, 131(17):171404, 2023.
- [32] Moslem Ahmadvand, Ligong Bian, and Soroush Shakeri. Heavy QCD axion model in light of pulsar timing arrays. *Phys. Rev. D*, 108(11):115020, 2023.
- [33] Haipeng An, Boye Su, Hanwen Tai, Lian-Tao Wang, and Chen Yang. Phase transition during inflation and the gravitational wave signal at pulsar timing arrays. *Phys. Rev. D*, 109(12):L121304, 2024.
- [34] Deng Wang. Constraining Cosmological Phase Transitions with Chinese Pulsar Timing Array Data Release 1. 7 2023.
- [35] Ricardo Z. Ferreira, Alessio Notari, Oriol Pujolas, and Fabrizio Rompineve. Gravitational waves from domain walls in Pulsar Timing Array datasets. *JCAP*, 02:001, 2023.
- [36] Naoya Kitajima, Junseok Lee, Kai Murai, Fuminobu Takahashi, and Wen Yin. Gravitational

- waves from domain wall collapse, and application to nanohertz signals with QCD-coupled axions. *Phys. Lett. B*, 851:138586, 2024.
- [37] Shu-Yuan Guo, Maxim Khlopov, Xuewen Liu, Lei Wu, Yongcheng Wu, and Bin Zhu. Footprints of Axion-Like Particle in Pulsar Timing Array Data and JWST Observations. 6 2023.
  - [38] Simone Blasi, Alberto Mariotti, Aäron Rase, and Alexander Sevrin. Axionic domain walls at Pulsar Timing Arrays: QCD bias and particle friction. *JHEP*, 11:169, 2023.
  - [39] Yann Gouttenoire and Edoardo Vitagliano. Domain wall interpretation of the PTA signal confronting black hole overproduction. 6 2023.
  - [40] Basabendu Barman, Debasish Borah, Suruj Jyoti Das, and Indrajit Saha. Scale of Dirac leptogenesis and left-right symmetry in the light of recent PTA results. *JCAP*, 10:053, 2023.
  - [41] Bo-Qiang Lu, Cheng-Wei Chiang, and Tianjun Li. Clockwork axion footprint on nanohertz stochastic gravitational wave background. *Phys. Rev. D*, 109(10):L101304, 2024.
  - [42] Xiu-Fei Li. Probing the high temperature symmetry breaking with gravitational waves from domain walls. 7 2023.
  - [43] Xiao Kang Du, Ming Xia Huang, Fei Wang, and Ying Kai Zhang. Did the nHZ Gravitational Waves Signatures Observed By NANOGraV Indicate Multiple Sector SUSY Breaking? 7 2023.
  - [44] Graciela B. Gelmini and Jonah Hyman. Catastrogenesis with unstable ALPs as the origin of the NANOGraV 15 yr gravitational wave signal. *Phys. Lett. B*, 848:138356, 2024.
  - [45] Zhao Zhang, Chengfeng Cai, Yu-Hang Su, Shiyu Wang, Zhao-Huan Yu, and Hong-Hao Zhang. Nano-Hertz gravitational waves from collapsing domain walls associated with freeze-in dark matter in light of pulsar timing array observations. *Phys. Rev. D*, 108(9):095037, 2023.
  - [46] John Ellis, Marek Lewicki, Chunshan Lin, and Ville Vaskonen. Cosmic superstrings revisited in light of NANOGraV 15-year data. *Phys. Rev. D*, 108(10):103511, 2023.
  - [47] Naoya Kitajima and Kazunori Nakayama. Nanohertz gravitational waves from cosmic strings and dark photon dark matter. *Phys. Lett. B*, 846:138213, 2023.
  - [48] Ziwei Wang, Lei Lei, Hao Jiao, Lei Feng, and Yi-Zhong Fan. The nanohertz stochastic gravitational wave background from cosmic string loops and the abundant high redshift massive galaxies. *Sci. China Phys. Mech. Astron.*, 66(12):120403, 2023.
  - [49] George Lazarides, Rinku Maji, and Qaisar Shafi. Superheavy quasistable strings and walls bounded by strings in the light of NANOGraV 15 year data. *Phys. Rev. D*, 108(9):095041, 2023.
  - [50] Astrid Eichhorn, Rafael R. Lino dos Santos, and João Lucas Miqueleto. From quantum gravity to gravitational waves through cosmic strings. *Phys. Rev. D*, 109(2):026013, 2024.
  - [51] Géraldine Servant and Peera Simakachorn. Constraining postinflationary axions with pulsar timing arrays. *Phys. Rev. D*, 108(12):123516, 2023.
  - [52] Stefan Antusch, Kevin Hinze, Shaikh Saad, and Jonathan Steiner. Singling out SO(10) GUT

- models using recent PTA results. *Phys. Rev. D*, 108(9):095053, 2023.
- [53] Bowen Fu, Anish Ghoshal, Stephen F. King, and Moinul Hossain Rahat. Type-I two-Higgs-doublet model and gravitational waves from domain walls bounded by strings. 4 2024.
- [54] Masaki Yamada and Kazuya Yonekura. Dark baryon from pure Yang-Mills theory and its GW signature from cosmic strings. *JHEP*, 09:197, 2023.
- [55] Shuailiang Ge. Stochastic gravitational wave background: birth from string-wall death. *JCAP*, 06:064, 2024.
- [56] Adeela Afzal et al. The NANOGrav 15 yr Data Set: Search for Signals from New Physics. *Astrophys. J. Lett.*, 951(1):L11, 2023.
- [57] John Ellis, Malcolm Fairbairn, Gabriele Franciolini, Gert Hütsi, Antonio Iovino, Marek Lewicki, Martti Raidal, Juan Urrutia, Ville Vaskonen, and Hardi Veermäe. What is the source of the PTA GW signal? *Phys. Rev. D*, 109(2):023522, 2024.
- [58] Yu-Mei Wu, Zu-Cheng Chen, and Qing-Guo Huang. Cosmological interpretation for the stochastic signal in pulsar timing arrays. *Sci. China Phys. Mech. Astron.*, 67(4):240412, 2024.
- [59] Jogesh C. Pati and Abdus Salam. Lepton Number as the Fourth Color. *Phys. Rev. D*, 10:275–289, 1974. [Erratum: *Phys.Rev.D* 11, 703–703 (1975)].
- [60] R. N. Mohapatra and Jogesh C. Pati. A Natural Left-Right Symmetry. *Phys. Rev. D*, 11:2558, 1975.
- [61] Rabindra N. Mohapatra and Jogesh C. Pati. Left-right gauge symmetry and an "isoconjugate" model of CP violation. *Phys. Rev. D*, 11:566–571, Feb 1975.
- [62] G. Senjanovic and Rabindra N. Mohapatra. Exact Left-Right Symmetry and Spontaneous Violation of Parity. *Phys. Rev. D*, 12:1502, 1975.
- [63] Goran Senjanovic. Spontaneous Breakdown of Parity in a Class of Gauge Theories. *Nucl. Phys. B*, 153:334–364, 1979.
- [64] Alessio Maiezza, Goran Senjanović, and Juan Carlos Vasquez. Higgs sector of the minimal left-right symmetric theory. *Phys. Rev. D*, 95(9):095004, 2017.
- [65] N. G. Deshpande, J. F. Gunion, B. Kayser, and Fredrick Olness. Left-right-symmetric electroweak models with triplet higgs field. *Phys. Rev. D*, 44:837–858, Aug 1991.
- [66] Goran Senjanovic. Is left-right symmetry the key? *Mod. Phys. Lett. A*, 32(04):1730004, 2017.
- [67] Rabindra N. Mohapatra and Deepinder P. Sidhu. Gauge Theories of Weak Interactions with Left-Right Symmetry and the Structure of Neutral Currents. *Phys. Rev. D*, 16:2843, 1977.
- [68] Ernest Ma. Particle Dichotomy and Left-Right Decomposition of E(6) Superstring Models. *Phys. Rev. D*, 36:274, 1987.
- [69] K. S. Babu, Xiao-Gang He, and Ernest Ma. New Supersymmetric Left-Right Gauge Model: Higgs Boson Structure and Neutral Current Analysis. *Phys. Rev. D*, 36:878, 1987.
- [70] Ernest Ma. Dark Left-Right Model: CDMS, LHC, etc. *J. Phys. Conf. Ser.*, 315:012006,

- 2011.
- [71] Mariana Frank, Benjamin Fuks, and Özer Özdal. Natural dark matter and light bosons with an alternative left-right symmetry. *JHEP*, 04:116, 2020.
  - [72] Mariana Frank, Chayan Majumdar, P. Poulose, Supriya Senapati, and Urjit A. Yajnik. Exploring  $0\nu\beta\beta$  and leptogenesis in the alternative left-right model. *Phys. Rev. D*, 102(7):075020, 2020.
  - [73] Lukáš Gráf, Sudip Jana, Ajay Kaladharan, and Shaikh Saad. Gravitational wave imprints of left-right symmetric model with minimal Higgs sector. *JCAP*, 05(05):003, 2022.
  - [74] Véronique Bernard, Sébastien Descotes-Genon, and Luiz Vale Silva. Constraining the gauge and scalar sectors of the doublet left-right symmetric model. *JHEP*, 09:088, 2020.
  - [75] Siddhartha Karmakar, Jai More, Akhila Kumar Pradhan, and S. Uma Sankar. Constraints on the doublet left-right symmetric model from Higgs data. *JHEP*, 03:168, 2023.
  - [76] U. A. Yajnik, Hatem Widyan, Debajyoti Choudhari, Shobhit Mahajan, and Amitabha Mukherjee. Topological defects in the left-right symmetric model and their relevance to cosmology. *Phys. Rev. D*, 59:103508, 1999.
  - [77] Debasish Borah and Arnab Dasgupta. Probing left-right symmetry via gravitational waves from domain walls. *Phys. Rev. D*, 106(3):035016, 2022.
  - [78] Joydeep Chakraborty, Rinku Maji, and Stephen F. King. Unification, Proton Decay and Topological Defects in non-SUSY GUTs with Thresholds. *Phys. Rev. D*, 99(9):095008, 2019.
  - [79] Sasmita Mishra and Urjit A. Yajnik. Spontaneously broken parity and consistent cosmology with transitory domain walls. *Phys. Rev. D*, 81:045010, 2010.
  - [80] Debasish Borah and Sasmita Mishra. Spontaneous R-parity breaking, Left-Right Symmetry and Consistent Cosmology with Transitory Domain Walls. *Phys. Rev. D*, 84:055008, 2011.
  - [81] Piyali Banerjee and Urjit Yajnik. Domain walls and CP violation with left right supersymmetry: implications for leptogenesis and electron EDM. *JHEP*, 07:039, 2021.
  - [82] Z. A. Borboruah and U. A. Yajnik. Left-Right Symmetry Breaking and Gravitational Waves : A Tale of Two Phase Transitions. 12 2022.
  - [83] Piyali Banerjee and Urjit A. Yajnik. Gravitational wave signature of generic disappearance of  $Z_2$ -symmetry breaking domain walls. *JHEP*, 01:007, 2024.
  - [84] Sergio Ferrando Solera, Antonio Pich, and Luiz Vale Silva. Direct bounds on Left-Right gauge boson masses at LHC Run 2. 9 2023.
  - [85] Siddhartha Karmakar and Dhruv Ringe. Gravitational wave imprints of the doublet left-right symmetric model. *Phys. Rev. D*, 109(7):075034, 2024.
  - [86] James M. Cline and Pierre-Anthony Lemieux. Electroweak phase transition in two higgs doublet models. *Physical Review D*, 55(6):3873–3881, mar 1997.
  - [87] Richard A. Battye, Gary D. Brawn, and Apostolos Pilaftsis. Vacuum Topology of the Two Higgs Doublet Model. *JHEP*, 08:020, 2011.
  - [88] Richard A. Battye, Apostolos Pilaftsis, and Dominic G. Viatic. Simulations of Domain Walls



- in Two Higgs Doublet Models. *JHEP*, 01:105, 2021.
- [89] Yongcheng Wu, Ke-Pan Xie, and Ye-Ling Zhou. Classification of Abelian domain walls. *Phys. Rev. D*, 106(7):075019, 2022.
- [90] Ken'ichi Saikawa. A review of gravitational waves from cosmic domain walls. *Universe*, 3(2):40, 2017.
- [91] Henry Lew and Antonio Riotto. Baryogenesis, domain walls and the role of gravity. *Phys. Lett. B*, 309:258–263, 1993.
- [92] Takashi Hiramatsu, Masahiro Kawasaki, and Ken'ichi Saikawa. Gravitational Waves from Collapsing Domain Walls. *JCAP*, 05:032, 2010.
- [93] Karsten Jedamzik. Big bang nucleosynthesis constraints on hadronically and electromagnetically decaying relic neutral particles. *Phys. Rev. D*, 74:103509, 2006.
- [94] Yang Bai and Mrunal Korwar. Cosmological constraints on first-order phase transitions. *Phys. Rev. D*, 105:095015, May 2022.
- [95] N. Aghanim et al. Planck 2018 results. VI. Cosmological parameters. *Astron. Astrophys.*, 641:A6, 2020. [Erratum: *Astron. Astrophys.* 652, C4 (2021)].
- [96] A. Vilenkin. Gravitational Field of Vacuum Domain Walls and Strings. *Phys. Rev. D*, 23:852–857, 1981.
- [97] John Preskill, Sandip P. Trivedi, Frank Wilczek, and Mark B. Wise. Cosmology and broken discrete symmetry. *Nucl. Phys. B*, 363:207–220, 1991.
- [98] S. Chang, C. Hagmann, and P. Sikivie. Studies of the motion and decay of axion walls bounded by strings. *Phys. Rev. D*, 59:023505, Dec 1998.
- [99] Takashi Hiramatsu, Masahiro Kawasaki, and Ken'ichi Saikawa. On the estimation of gravitational wave spectrum from cosmic domain walls. *JCAP*, 02:031, 2014.
- [100] Michele Maggiore. Gravitational wave experiments and early universe cosmology. *Phys. Rept.*, 331:283–367, 2000.
- [101] Chiara Caprini and Daniel G. Figueroa. Cosmological Backgrounds of Gravitational Waves. *Class. Quant. Grav.*, 35(16):163001, 2018.
- [102] Mohan Rajagopal and Roger W. Romani. Ultra–Low-Frequency Gravitational Radiation from Massive Black Hole Binaries. *Astrophys. J.*, 446:543, June 1995.
- [103] A. H. Jaffe and D. C. Backer. Gravitational waves probe the coalescence rate of massive black hole binaries. *The Astrophysical Journal*, 583(2):616, feb 2003.
- [104] J. Stuart B. Wyithe and Abraham Loeb. Low-frequency gravitational waves from massive black hole binaries: Predictions for lisa and pulsar timing arrays. *The Astrophysical Journal*, 590(2):691, jun 2003.
- [105] Alberto Sesana, Francesco Haardt, Piero Madau, and Marta Volonteri. Low-frequency gravitational radiation from coalescing massive black hole binaries in hierarchical cosmologies. *The Astrophysical Journal*, 611(2):623, aug 2004.
- [106] Sarah Burke-Spolaor, Stephen R. Taylor, Maria Charisi, Timothy Dolch, Jeffrey S. Hazboun,

- A. Miguel Holgado, Luke Zoltan Kelley, T. Joseph W. Lazio, Dustin R. Madison, Natasha McMann, Chiara M. F. Mingarelli, Alexander Rasskazov, Xavier Siemens, Joseph J. Simon, and Tristan L. Smith. The astrophysics of nanohertz gravitational waves. *The Astronomy and Astrophysics Review*, 27(1):5, Jun 2019.
- [107] Andrea Mitridate. Ptarcade. Apr 2023.
- [108] Andrea Mitridate, David Wright, Richard von Eckardstein, Tobias Schröder, Jonathan Nay, Ken Olum, Kai Schmitz, and Tanner Trickle. PTArcade. 6 2023.
- [109] Justin A. Ellis, Michele Vallisneri, Stephen R. Taylor, and Paul T. Baker. ENTERPRISE: Enhanced Numerical Toolbox Enabling a Robust PulsAR Inference Suite, September 2020.
- [110] Eric Thrane and Joseph D. Romano. Sensitivity curves for searches for gravitational-wave backgrounds. *Phys. Rev. D*, 88(12):124032, 2013.
- [111] A. Weltman et al. Fundamental physics with the Square Kilometre Array. *Publ. Astron. Soc. Austral.*, 37:e002, 2020.
- [112] Alberto Sesana et al. Unveiling the gravitational universe at  $\mu$ -Hz frequencies. *Exper. Astron.*, 51(3):1333–1383, 2021.
- [113] Pau Amaro-Seoane et al. Laser Interferometer Space Antenna. 2 2017.
- [114] Vincent Corbin and Neil J. Cornish. Detecting the cosmic gravitational wave background with the big bang observer. *Class. Quant. Grav.*, 23:2435–2446, 2006.
- [115] Naoki Seto, Seiji Kawamura, and Takashi Nakamura. Possibility of direct measurement of the acceleration of the universe using 0.1-Hz band laser interferometer gravitational wave antenna in space. *Phys. Rev. Lett.*, 87:221103, 2001.
- [116] Benjamin P Abbott et al. Exploring the Sensitivity of Next Generation Gravitational Wave Detectors. *Class. Quant. Grav.*, 34(4):044001, 2017.
- [117] M. Punturo et al. The Einstein Telescope: A third-generation gravitational wave observatory. *Class. Quant. Grav.*, 27:194002, 2010.
- [118] Kai Schmitz. New Sensitivity Curves for Gravitational-Wave Experiments, February 2020.